AIP | Physics of Fluids

Instabilities in the spin-up of a rotating, stratified fluid

R. J. Munro, M. R. Foster, and P. A. Davies

Citation: Physics of Fluids **22**, 054108 (2010); doi: 10.1063/1.3422554

View online: http://dx.doi.org/10.1063/1.3422554

View Table of Contents: http://scitation.aip.org/content/aip/journal/pof2/22/5?ver=pdfcov

Published by the AIP Publishing

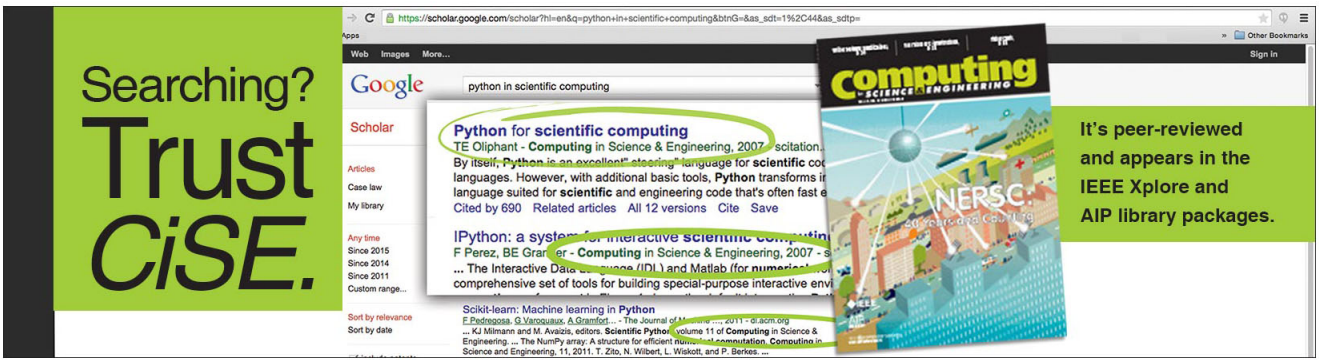

Instabilities in the spin-up of a rotating, stratified fluid

R. J. Munro,[1,a)] M. R. Foster,[2] and P. A. Davies[3]
[1]*Environmental Fluid Mechanics Research Group, Process and Environmental Research Division, Faculty of Engineering, University of Nottingham, Nottingham NG7 2RD, United Kingdom*
[2]*Department of Aerospace Engineering, The Ohio State University, Columbus, Ohio 43210, USA*
[3]*Department of Civil Engineering, University of Dundee, Dundee DD1 4HN, United Kingdom*

(Received 23 June 2009; accepted 13 April 2010; published online 26 May 2010)

Theoretical analyses and laboratory experiments have been performed on the stability of a flow generated by the differential cyclonic corotation of a flat, rigid disk in a uniformly rotating, linearly stratified fluid contained within a cylindrical tank. The undisturbed fluid is stably stratified with salt (Schmidt number $\sigma \approx 670$) and the (vertical) axes of rotation of the disk and the fluid container are coincident. The theoretical analysis shows that when the interior flow satisfies gradient wind balance (or, alternatively, thermal wind balance), it is destabilized by the action of viscosity. In the experiments, the manifestation of the viscous overturning instability is seen to be the formation of steplike internal microstructures in the density field, observed as regularly spaced, curved ring-shaped sheets with associated localized sharp, vertical density gradients. A stability analysis of the flow shows that the instability criterion is dependent on local values of the vertical and radial gradients of zonal velocity and the background density field. These quantities are measured in the experiments using a combination of horizontal-plane particle image velocimetry and an array of traversing microconductivity probes. The stability criterion based on this linear analysis predicts that the interior of the fluid is unstable. Using the $\sigma \gg 1$ condition, simple asymptotic expressions for the maximum growth rate and associated wave number have been derived from the cubic dispersion relation. The theoretically predicted length scales and e-folding times associated with the fastest growing modes are found to give excellent agreement with the corresponding values obtained from the laboratory experimental data. © *2010 American Institute of Physics*. [doi:10.1063/1.3422554]

I. INTRODUCTION

The term spin-up is commonly used to describe the process by which a bounded fluid in a state of solid-body rotation responds to a change in external forcing induced by an increase in rotation rate of the flow boundaries (or, in some cases, a specific region of the flow boundary). Given the significance of spin-up to the dynamics controlling many atmospheric and oceanographic flows (in which the effects associated with the Earth's rotation are important and often dominant), a considerable amount of research has been dedicated to analyzing the spin-up problem for both homogeneous and stratified fluids, as well as for a range of flow geometries and configurations. Much of this previous work to date is described in the review articles by Benton and Clarke[1] and, more recently, by Duck and Foster.[2]

This article further investigates the "double-diffusive" instability associated with the spin-up of a stably stratified fluid; a mechanism first identified by McIntyre.[3,4] The experiment configuration we use to study this instability (described in detail in Sec. III) consists of a cylindrical tank containing a stably stratified water solution which is initially in a state of solid rotation, with the axis of rotation coincident with the central symmetry axis of the cylinder. At time $t=0$, relative motion within the fluid is induced by the rotation of a smooth, flat, rigid, horizontal disk positioned at the tank base and set to rotate uniformly, coaxially, and cyclonically (viz., in the same direction as the background rotation). Various processes have been studied using this, similar or related configurations. Typical examples include theoretical aspects of stratified spin-up,[5,6] mixing and frontogenesis,[7–11] and internal waves.[12]

McIntyre[3] discovered the theoretical basis of the double-diffusive instability when investigating the properties of a steady axisymmetric zonal shear flow in a thermally stratified annulus. Local linear stability theory was used to show that when the background flow is in geostrophic balance, and provided that $\sigma \neq 1$ (where for thermal and saline stratifications σ denotes the Prandtl and Schmidt numbers, respectively), the flow can be destabilized by the disparity in diffusion coefficients of momentum and density of the fluid, giving rise to relatively small-scale axisymmetric overturning motions.

At about the same time, and using an experiment setup similar to one the described here, Baker[13] provided experimental evidence of McIntyre's instability for a salt-stratified fluid. Baker[13] used the shadowgraph technique to visualize the instability, which manifests itself as a regular density step (or staircase) microstructure superimposed on the background density field. [A shadowgraph image showing a typical density microstructure observed in our experiments is given in Fig. 5(a).] Baker[13] used measurements obtained directly from the shadowgraph images to compare with McIntyre's instability criteria for the $\sigma \gg 1$ limit. A similar

[a)]Electronic mail: rick.munro@nottingham.ac.uk. Telephone: +44 (0)115 9513893.

analysis was performed by Calman,[14] although improved experimental data were obtained using a single conductivity probe (to sample the fluid density field) and dye lines (to estimate the zonal velocity field). (There is also speculative evidence for the occurrence of this double-diffusive instability in the study by Hedstrom and Armi.[15])

This paper describes experiments used to investigate, in detail, the development of McIntyre's diffusive instability. Following the approach of Baker,[13] our experiments consider the spin-up of a linearly stratified, salt water solution by the differential rotation of a horizontal disk. The focus was on obtaining detailed measurements of how the fluid density and velocity fields (and associated gradients) develop as the instability forms, with an emphasis on obtaining significantly improved spatial and temporal resolution in comparison with the relatively primitive measurements obtained by Baker[13] and Calman.[14] This was achieved using an array of high-frequency response conductivity probes to measure the fluid density field and particle image velocimetry (PIV) to measure the zonal-plane velocity field (at different heights within the fluid). McIntyre's linear stability theory is also reformulated in the context of this experimental setup. We then use the dispersion relation in the $\sigma \gg 1$ limit to derive asymptotic results for the most unstable normal mode. Maximum growth rates and corresponding wave numbers are then compared with observations.

II. LINEAR STABILITY THEORY

In anticipation of the cylindrical geometry used in our experiments, let (r,θ,z) denote the cylindrical coordinate system which rotates with constant angular velocity $\Omega\hat{z}$ about the vertical z-axis aligned antiparallel to the gravitational acceleration vector $-g\hat{z}$. Relative to this rotating reference frame, we consider a steady, axisymmetric zonal shear flow $\boldsymbol{u}(r,z)=\bar{v}(r,z)\hat{\boldsymbol{\theta}}$ of continuously salt-stratified water solution which is Boussinesq and in hydrostatic and gradient wind balance. [In this context, the term Boussinesq indicates that density variations are assumed negligible except in the buoyancy terms, and that the coefficients of viscosity (ν), salinity diffusion (κ), and salinity contraction (β) are taken to be constant (with frictional heating assumed negligible).] Moreover, we write the (dimensional) density and pressure fields as

$$\rho(r,z) = \rho_s(z) + \rho_0\beta\bar{s}(r,z), \tag{1a}$$

$$p(r,z) = p_s(z) + \bar{p}(r,z), \tag{1b}$$

where $\rho_s(z)$ and $p_s(z)$ denote the hydrostatic components, ρ_0 is a constant reference density, and $\bar{s}(r,z)$ is the dimensionless salinity. The gradient wind balance (or zonal vorticity equation), therefore, is given by

$$2(\Omega + \bar{v}/r)\bar{v}_z = -g\beta\bar{s}_r, \tag{2}$$

where the subscript partial-derivative notation is standard. This basic flow-state will be assumed to remain stably stratified $(\bar{s}_z<0)$ and centrifugally stable $(\bar{v}_r>0)$ throughout. Note that the cylindrical nature of the flow means that Eq. (2) includes the nonlinear (centrifugal) term $2\bar{v}_z\bar{v}/r$, which is required to maintain the balanced state when the isobars are curved. However, it is worth noting that when curvature effects are negligible, Eq. (2) reduces to the thermal wind equation $2\Omega\bar{v}_z=-g\beta\bar{s}_r$, which corresponds to the geostrophic balance. Indeed, it is this thermal wind balance that was used in the analysis of both McIntyre[3] and Calman.[14] However, it should be noted that the analysis which follows here is little affected by whether the background state is taken to be a gradient wind or a thermal wind balance.

McIntyre[3] showed that the basic balanced state described by Eqs. (1) and (2), when otherwise stable according to the classical inviscid criterion, can become unstable provided that $\sigma=\nu/\kappa\neq 1$. In the present case, that of a salt-stratified water solution with Schmidt number $\sigma\approx 670$, the destabilizing agent is viscosity. That is, the relative absence of salinity diffusion (in comparison with momentum diffusion) means that a fluid element that is perturbed from its initial balanced state will be brought into momentum equilibrium by the action of viscous torques significantly faster than the density of the element is able to adjust to the ambient buoyancy of its new surroundings. Therefore, any local density difference induced by this double-diffusive mechanism can give rise to meridional overturning motions (i.e., zonal vorticity), the basic source of this instability. Moreover, the instability mechanism is of a localized nature, not requiring for its function the presence of a flow boundary, or a free surface. Hence, adopting the approach taken by McIntyre,[3] we treat the basic flow as being unbounded and consider the local behavior of small-amplitude, axisymmetric perturbations about the background balanced state described by Eqs. (1) and (2).

The basic steady state is localized about an interior point (r_0,z_0) by introducing dimensionless meridional coordinates (x,y) and time τ defined, respectively, by

$$x=(r-r_0)/\delta_1, \quad y=(z-z_0)/\delta_1, \quad \tau=t/\tau_1, \tag{3}$$

where the dimensional time and length scales τ_1 and δ_1 are chosen such that

$$\tau_1=(g\beta\bar{s}_r^0)^{-1/2}, \quad \delta_1=(\nu/2\Omega)^{1/2}\gamma^{-1/4}, \tag{4}$$

with the dimensionless parameter γ defined as

$$\gamma=g\beta\bar{s}_r^0/4\Omega^2. \tag{5}$$

In the above, the notation $\bar{s}^0=\bar{s}(r_0,z_0)$ has been used, and will henceforth be adopted throughout, together with $\bar{v}^0=\bar{v}(r_0,z_0)$. [Note that using the balanced state given in Eq. (2), we can also write $\gamma=-(\Omega r_0+\bar{v}^0)\bar{v}_z^0/2r_0\Omega^2$, and that γ is the analogue of the dimensionless parameter defined in Eq. (2.4d) of McIntyre[3] (p. 24).]

The background flow variables are then expanded about the interior point (r_0,z_0) as $\bar{v}=\bar{v}^0+\epsilon r_0(x\bar{v}_r^0+y\bar{v}_z^0)$ (likewise for $\bar{s}$, $\bar{v}_r$, $\bar{s}_r$, $\bar{v}_z$, and $\bar{s}_z$), where $\epsilon=\delta_1/r_0$ and $\epsilon\ll 1$ is assumed. Therefore, neglecting terms $\mathcal{O}(\epsilon)$ [and noting that $1/r=1/r_0(1+\epsilon x)=1/r_0+\mathcal{O}(\epsilon)$], the linearized equations for perturbations in momentum and density, about (r_0,z_0), can be written in dimensionless form as

$$\left(\frac{\partial}{\partial\tau}-\nabla^2\right)\nabla^2\psi - v_y - s_x = 0, \tag{6a}$$

$$\left(\frac{\partial}{\partial\tau}-\nabla^2\right)v-(\Theta_1\psi_y-\psi_x)=0, \tag{6b}$$

$$\left(\frac{\partial}{\partial\tau}-\sigma^{-1}\nabla^2\right)s-(\Theta_2\psi_x-\psi_y)=0, \tag{6c}$$

where $(\psi_y, v, -\psi_x)$ and s denote (dimensionless) perturbations in velocity and salinity, respectively, (each of which are assumed to be axisymmetric functions of x, y, and τ), and $\nabla^2 \equiv \partial^2/\partial x^2 + \partial^2/\partial y^2$ is the standard Laplacian. Using continuity, the stream function $\psi(x,y,\tau)$ has been introduced to eliminate the dependence on the pressure perturbation by combining the radial and vertical momentum equations (using cross-differentiation) into the single Eq. (6a) for the zonal component of vorticity, $\nabla^2\psi$. The dimensionless coefficient parameters in Eqs. (6) are defined as

$$\sigma = \nu/\kappa, \tag{7a}$$

$$\Theta_1 = (\bar{v}_r^0 + \bar{v}^0/r_0 + 2\Omega)/\bar{v}_z^0, \tag{7b}$$

$$\Theta_2 = (\bar{s}_z^0 - N_0^2/\beta g)/\bar{s}_r^0, \tag{7c}$$

which depend only on the system constants (ν,κ,Ω), the buoyancy frequency $N_0=[-(g/\rho_0)\mathrm{d}\rho_s/\mathrm{d}z]^{1/2}$, and the local characteristics of the zonal flow and salinity fields. Finally, note that the final form of Eqs. (6) are obtained by choosing the relative scales for the perturbation amplitudes such that

$$2(\bar{v}^0/r_0+\Omega)v^* = \psi^*/(\tau_1\delta_1) = g\beta s, \tag{8}$$

where the star superscript denotes the dimensional form the perturbation variables.

The linearized Eqs. (6) support simple normal mode solutions of the form

$$(\psi, v, s) = \exp[ik(x\cos\phi + y\sin\phi) + \omega\tau], \tag{9}$$

where the growth rate ω (which can be complex) is dependent on the wavenumber k and the wave-vector direction ϕ (both of which are real). The basic state $(\sigma,\Theta_1,\Theta_2)$ is therefore unstable if there exist values of (k,ϕ) such that $\Re(\omega)>0$. Substituting Eq. (9) into Eqs. (6) and setting the determinant of the resulting coefficient matrix to zero gives a cubic dispersion relation of the form

$$(\omega+k^2)^2(\omega+k^2/\sigma)+(\mathcal{I}+\mathcal{G})\omega+(\mathcal{I}/\sigma+\mathcal{G})k^2=0, \tag{10}$$

where

$$\mathcal{I} = \tfrac{1}{2}\sin 2\phi - \Theta_1\sin^2\phi, \tag{11a}$$

$$\mathcal{G} = \tfrac{1}{2}\sin 2\phi - \Theta_2\cos^2\phi, \tag{11b}$$

which depend only on the background flow characteristics and ϕ.

The form of the dispersion relation (10) is the same as that derived by McIntyre,[3] and we now take advantage of McIntyre's analysis of Eq. (10). First, we see that the necessary criterion for classically subcritical flow to be $\mathcal{I}+\mathcal{G}>0$ for all values of ϕ; since by putting $k=0$ in Eq. (10) with this condition we then obtain the roots $\omega=0, \pm i(\mathcal{I}+\mathcal{G})^{1/2}$. Moreover, McIntyre shows that for this classically subcritical flow (i.e., with $\mathcal{I}+\mathcal{G}>0$ assumed), the necessary criterion for the diffusive instability described above can be obtained by considering the real root of Eq. (10)

$$\omega = -k^2(\mathcal{I}/\sigma+\mathcal{G})/(\mathcal{I}+\mathcal{G}) + \mathcal{O}(k^6), \tag{12}$$

where we have taken $k \ll 1$ for this approximation.

Specifically, there is monotonic instability if and only if there exist values of ϕ such that $\Re(\omega)>0$. Using Eq. (12), this condition at leading order reduces to $\mathcal{I}/\sigma+\mathcal{G}<0$, which gives

$$\Theta_1\Theta_2 < \frac{\sigma}{4}\left(1+\frac{1}{\sigma}\right)^2. \tag{13}$$

Furthermore, oscillatory instability occurs if and only if there exist ϕ such that $\Re(\omega)>-k^2(2+1/\sigma)$ (for details, see McIntyre[3]). Again, using Eq. (12), this condition at leading order becomes $\mathcal{I}/\sigma+\mathcal{G}>(2+1/\sigma)(\mathcal{I}+\mathcal{G})$, which gives

$$\Theta_1\Theta_2 < \frac{9}{8}\left\{\frac{[1+(1/3\sigma)]^2}{1+(1/\sigma)}\right\}. \tag{14}$$

We return to these theoretical results in Sec. IV, with analysis of the limiting case for large Schmidt number σ.

III. EXPERIMENTS

A. Experiment arrangement

Figure 1 shows a side view of the experiment apparatus. A cylindrical acrylic tank (diameter 36 cm; height 30 cm) was fitted centrally inside an outer rectangular container (thereby eliminating optical distortion caused by the curved sidewalls) and mounted on a rotating turntable with the axis of the cylinder aligned through the vertical rotation axis of the table (as shown). With the table initially stationary, the two tanks were filled to a depth $H=25$ cm with a linearly salt-stratified water solution using the standard double-bucket system.[16,17] Once filled and the fluid quiescent, the system was gradually brought to a state of solid-body rotation, with the desired angular frequency Ω. To prevent excessive mixing, the prescribed final solid rotation rate of the system (Ω) was attained using small incremental increases from rest over a time interval of about 7 hours.

Following the approach of Baker,[13] the flow conditions required to observe the instability were established using a smooth disk of radius $R=17.5$ cm (and negligible thickness), set to rotate horizontally at the base of the cylindrical tank about a drive shaft mounted through the central axis of cylinder (see Fig. 1). The drive shaft was connected (via a water-tight seal) to an external motor positioned below the two tanks, allowing the disk to be rotated independently of the table with a predetermined (constant) angular frequency Ω_d. The disk rotation (in the same sense as the background rotation of the system) was initiated at time $t=0$, with the fluid in a state of solid rotation. Our cylindrical coordinates (r,θ,z) are aligned so that the horizontal disk surface corresponds to $z=0$, with the vertical z-axis directed through the central axis of the cylinder. In all cases, the time taken for the disk to reach a steady rotation rate was significantly less than one table rotation period $(2\pi/\Omega)$.

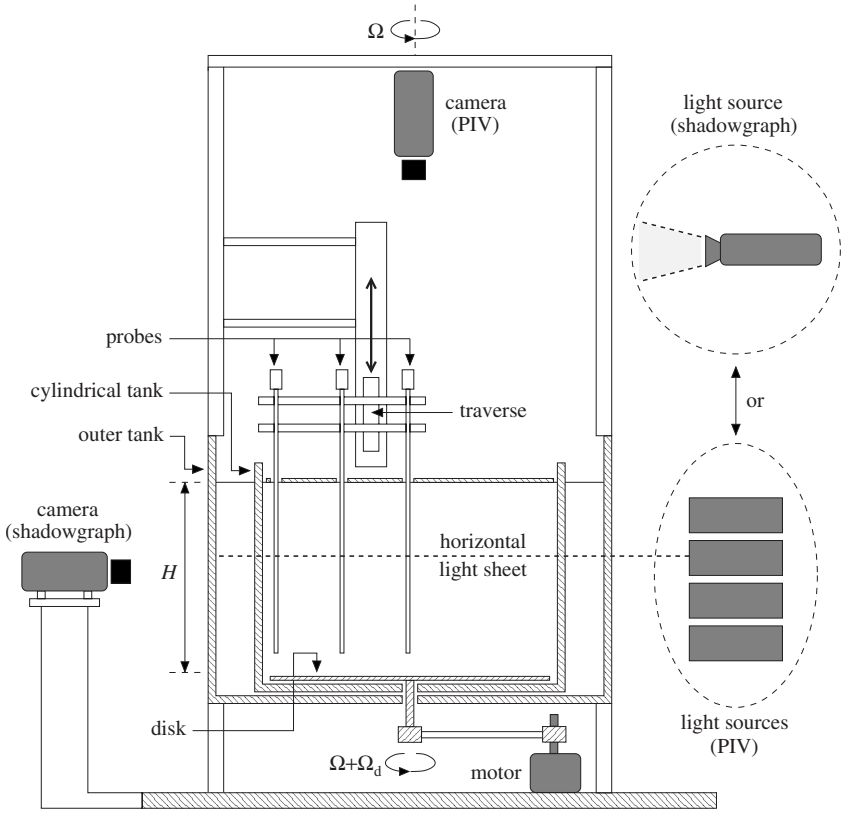

FIG. 1. Sketch showing the experiment apparatus.

Measurements of vertical profiles of fluid density were obtained using an array of three conductivity probes[18] fitted on a vertical, motor-driven traverse mechanism above the cylinder, at radii $r/R=0,0.5,0.9$ (see Fig. 1). A personal computer (PC) mounted on the turntable controlled the motion of the traverse, together with acquisition and storage of the conductivity and probe-position data. When idle, the probes were located above the fluid with only the sampling tip submerged below the fluid surface. A single traverse measured the vertical structure of fluid density over the range $0.04 \leq z/H \leq 0.90$ (during the downward stroke only), at these three radial locations. The traverse time and sampling frequency of the probes were 1.5 s and 200 Hz, respectively, giving density measurements approximately every 0.08 cm. The correspondence between conductivity and density was established empirically before each experiment, using a simple calibration procedure. During the initial period following the onset of disk rotation, density measurements were taken at intervals of between 30 s and 2 min. The sampling frequency was progressively reduced throughout the experiment, as the flow conditions became quasisteady, to intervals of between 20 and 30 min during the later stages of the experiment.

The primary source of uncertainty in the density measurements was associated with inherent signal noise and the empirical conversion between conductivity to density. In all cases, the resulting variability in the density measurements obtained with the probes was negligible (and always less than 10^{-3} g/cm^3). Uncertainties in the probe response induced by thermal variations in the fluid (over the period of each experiment), and the variability associated with the mechanical measurements of probe position, were both found to be negligible in comparison to the above. (It is worth noting that the water used to fill the tanks was first allowed to reach the ambient temperature of the laboratory over a period of 24 hours; typical variations in the fluid temperature over the period of each experiment were always less than 1 °C.)

Measurements of the zonal velocity field were obtained, in four horizontal layers above the disk, using PIV. Small, neutrally buoyant tracer particles used to seed the fluid were illuminated by four horizontal light sheets positioned at fixed heights $z/H=0.12$, 0.32, 0.52, and 0.72 (see Fig. 1). A cyclic timing device activated each light sheet individually (for a set period of 30 s), while the remaining lights were switched off. This sequence was repeated indefinitely. The particle trajectories were recorded during each 30 s interval using a digital video camera (sampling at 24 Hz with 1380×512 pixel resolution) fastened to the turntable and positioned to view vertically down into the tank interior through a thin perspex lid used to eliminate free-surface distortion (see Fig. 1). The PC mounted on the turntable was used for image acquisition and storage, with the velocity fields calculated at the end of the experiment using PIV techniques developed by Dalziel.[19] At each of the four fixed heights, the processed velocity data, denoted by $u_1(x,y,t)\boldsymbol{i} + u_2(x,y,t)\boldsymbol{j}$, were first calculated in terms of the Cartesian coordinates system $x=r\cos\theta$, $y=r\sin\theta$, and then converted to corresponding polar coordinates, denoted $U(r,\theta,t)\hat{\boldsymbol{r}} + V(r,\theta,t)\hat{\boldsymbol{\theta}}$, using the standard transformation

$$\begin{pmatrix} U \\ V \end{pmatrix} = \begin{pmatrix} \cos\theta & \sin\theta \\ -\sin\theta & \cos\theta \end{pmatrix} \begin{pmatrix} u_1 \\ u_2 \end{pmatrix}. \tag{15}$$

The axisymmetric zonal velocity profiles $\bar{v}(r,z)$, at each of the four sample heights, were obtained by first time-averaging each $V(r,\theta,t)$ over the 30 s exposure period and then averaging azimuthally. Applying the same procedure to $U(r,\theta,t)$ gave $\bar{u}(r,z)\approx 0$ (thus demonstrating the axisymmetric nature of the flow in the interior region). Error bars illustrating the typical rms variability associated with these combined averaging procedures will be included in the velocity data, when presented in the following sections. Uncertainties associated with the PIV processing were negligible in comparison.

Note also that the conductivity probes could not be used in the seeded fluid required for the application of PIV due to interference caused by the tracer particles with the probe tips. Experiments, therefore, were repeated in pairs (one to obtain density measurements and one for velocity measurements). Care was taken to ensure that each pair of experiments was performed under the same conditions, and that the velocity and density measurements were obtained at coincident times in each case. In a selected number of the density experiments, the shadowgraph method[20] was also used to visualize the density perturbation field. Images were captured using the digital video camera (described above) mounted horizontally on the table, with the fluid body illuminated by a projected light source directed horizontally through the opposite wall of the tank (see Fig. 1). These images were not used for the purpose of quantitative measurements, but solely to visualize the features of the fluid density field.

In all experiments, the fluid depth above the disk surface H was kept fixed at 25 cm with Ω varied from 0.1 to 0.5 rad/s. The hydrostatic fluid density field $\rho_s(z)$ was always stably and approximately linearly stratified with initial buoyancy frequency $N_0=[-(g/\rho_0)\mathrm{d}\rho_s/\mathrm{d}z]^{1/2}$ ranging between 1.0 and 2.0 1/s, ρ_0 denoting the value of $\rho_s(z)$ at $z=0$. Note that when N_0 was compared with corresponding buoyancy frequency measured during the solid rotation state, no significant differences were evident. Of course, a state of purely static equilibrium cannot exist in the solid rotation state[21,22] (viz., the parabolic isosurfaces of salinity and pressure that are necessary for a contained, stratified fluid to be in a state of pure solid rotation, are not solutions of the corresponding salinity equation, $\kappa\nabla^2\bar{s}=0$, when $\kappa\neq 0$). However, for the experiments described in this article, with Froude number $Fr=\Omega^2R/g\lesssim 10^{-2}$, the resulting small-scale centrifugal convective circulations are very weak and have a negligible effect.

The disk rotation was always cyclonic with Ω_d ranging from 0.2 to 1.0 rad/s. In all cases considered, $2.0\leq N_0/\Omega\leq 20$ and $1.0\leq N_0/\Omega_d\leq 5.0$. Corresponding values of the Rossby number $Ro=\Omega_d/2\Omega$ were in the range 0.2–2.0, with the mid-disk Reynolds number $Re_m=\Omega_d R^2/4\nu$ between 1700 and 7500. For the range of salt concentrations used, the kinematic viscosity ν and the molecular diffusivity of salt κ were effectively constant at 0.01 and 1.5×10^{-5} cm^2/s, respectively, giving a constant Schmidt number of $\sigma=\nu/\kappa\approx 670$. Each experiment was run for between 15 and 24 hours. Table I shows a selection of typical experiment parameters. Of the four experiments shown, the diffusive instability was observed to occur *only* in experiments A and B. These four experiments will henceforth be used to illustrate our discussion throughout. Of course, the mechanism for McIntyre's viscous overturning instability is the same for all $\sigma>1$. However, we did not attempt to vary σ in our experiments. It should be noted, however, that in the experiments by Baker[13] and Calman,[14] the Schmidt number was varied between $310<\sigma<1800$, and the instability was observed to form within this range (provided, of course, the necessary instability criteria was satisfied).

TABLE I. A selection of four experiments chosen to illustrate the parameter ranges in which the diffusive instability was observed (A and B) and was not observed (C and D).

Experiment label	Ω (rad/s)	Ω_d (rad/s)	N_0 (1/s)	Ro	N_0/Ω
A	0.31	0.23	1.0	0.37	3.2
B	0.50	0.23	1.7	0.23	3.4
C	0.12	0.25	1.0	1.0	8.3
D	0.26	0.97	1.3	1.9	5.0

B. Observations

Before discussing the instability formation, we first describe how the required flow conditions are established. At $t=0$ the disk motion is initiated, with the container sidewalls remaining stationary relative to the rotating frame. The resulting spin-up processes thereafter establish two regions of flow, denoted I and II, which are shown schematically in Fig. 2; the left-hand and right-hand halves of the diagram depict the early and later stages of the flow development, respectively.

After several rotation periods, a thin boundary layer is established above the disk surface wherein the fluid is accelerated and spun-up by the action of viscous stresses. No longer stationary relative to the rotating frame, the boundary-layer fluid is forced radially outward by Coriolis acceleration and replaced with lighter fluid from the overlying interior by Ekman suction.[22,23] On encountering the container sidewall, the radial flux is forced upward into the lighter interior, establishing a local adverse vertical density gradient which overturns the fluid, forming a secondary meridional circulation. Initially, therefore, the spun-up fluid forms the frontal region, I, confined to the lower corners of the container [see Fig. 2(a)] consisting of the heaviest fluid, originally positioned above the disk. The vertical extent of the front is determined by the relative strength of the background stratification (N/Ω).

Region II consists of the interior fluid above the boundary layer and region I. Henceforth, BB' will be used to denote the interface between regions I and II, while AB' will denote the early stage interface between the boundary layer and region II [as shown in Fig. 2(a)]. Vertical Ekman suction increases cyclonic vorticity inside region II (by stretching the background vorticity), thereby generating zonal velocity, the

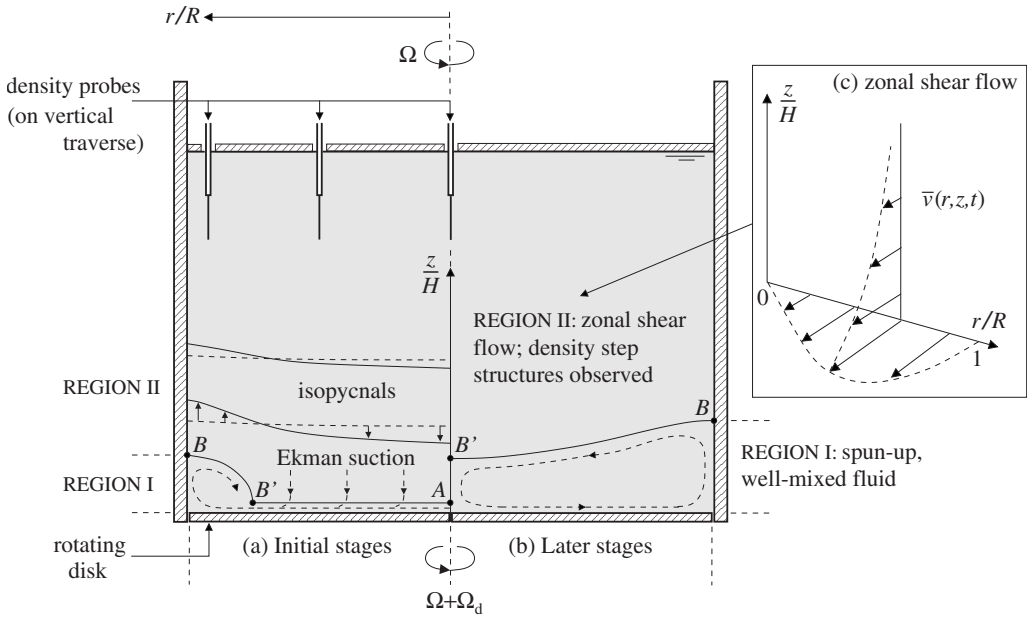

FIG. 2. Schematic showing the important flow characteristics leading to the development of the flow regions I and II (see text for description). The left-hand and right-hand halves of the diagram show the early and later stages of the flow development. The inset (c) illustrates the form of the axisymmetric zonal shear flow $\bar{v}(r,z,t)$ observed in region II.

magnitude of which decreases with height z, with the fluid furthest above the disk remaining largely unaffected. A schematic illustration of the induced zonal shear flow established in region II is shown in Fig. 2(c). Furthermore, directly above AB', Ekman suction acts to deform the initial, near-planar isopycnals downward, whereas above the developing corner front (region I) they are forced upward, as depicted in Fig. 2(a). Again, far above the disk surface, the isopycnals remain largely unaffected.

The features described above are readily identified in Figs. 3 and 4, which show (or include) data obtained from experiment A after $n=(\Omega/2\pi)t=9$ rotation periods ($t\approx 3$ min). In particular, note the direction in which the density profiles are deformed relative to the initial linear state (Fig. 3), with the initial formation of region I evident at $r/R=0.9$, for $z/H\leq 0.15$ (below which the fluid is well-mixed). Also note the form of the axisymmetric zonal shear flow $\bar{v}(r,z,t)$, with $\bar{v}_z<0$ and the no-slip condition establishing a region in which $\bar{v}_r<0$ near the tank sidewalls (Fig. 4).

The processes described above continue, causing region I to expand radially inward as it is supplied (via the boundary layer) with fluid from region II, the density of which is gradually decreasing with time. In doing so, the contact area AB' between the boundary layer and region II gets progressively smaller, thereby reducing the radial flux and the vertical Ekman suction on region II. Eventually, region I expands to cover the area above disk surface (i.e., $AB'=0$), as depicted in Fig. 2(b). At this point, the direct supply of interior fluid to region I via the disk boundary layer (and Ekman suction) is effectively switched off, whereafter lighter fluid from region II is entrained directly through the interface BB' by diffusion, reducing the rate at which the fluid in region II is spun-up. In experiment A, this event occurs after $n\approx 120$ rotation periods ($t\approx 42$ min). After this time, the interior region II flow is essentially quasisteady, while the interface BB' migrates slowly upward through the fluid. The small velocity difference between the disk surface and the fluid below BB' maintains a weak, secondary meridional circulation in region I.

The later stages of the flow development for experiment A are shown in Figs. 4 and 5, after $n=720$ rotation periods ($t\approx 4$ hours). The interface BB' is now clearly evident in each density profile at $z/H\approx 0.25$, below which the fluid is essentially well-mixed and largely spun-up [see Fig. 4(d)]. It is worth noting here that when Experiment A was terminated after 24 hours ($n=4125$), the interface BB' had only advanced to a position at $z/H\approx 0.45$. Also note in Fig. 4 the marked decrease in the rate at which the fluid in region II is spun-up during the period between $n=120$ and 720, in comparison with the rate observed during the early stages between $n=9$ and 120, when the Ekman dynamics are prevalent. This quasisteady nature of the interior flow is further confirmed by Fig. 6, showing the temporal development of the zonal flow field $\bar{v}(r,z,t)$ at the mid-disk radius $r/R=0.5$.

In Figs. 5(a) and 5(c), the regular steplike perturbations to the near-linear background density stratification (in region II) are the manifestation of the axisymmetric viscous overturning instability identified by McIntyre.[3] We now focus our attention on region II and describe how this density microstructure is observed to form. For further details regarding the dynamics leading to the formation of region I, the reader is referred to related numerical and experimental studies.[9–12]

In Sec. II we presented the linear theory to describe this diffusive instability mechanism. Recall that a basic requirement of this theory was for the background flow to be in the balanced state represented by Eq. (2). Indeed, over the range of conditions considered in this article, the instability was

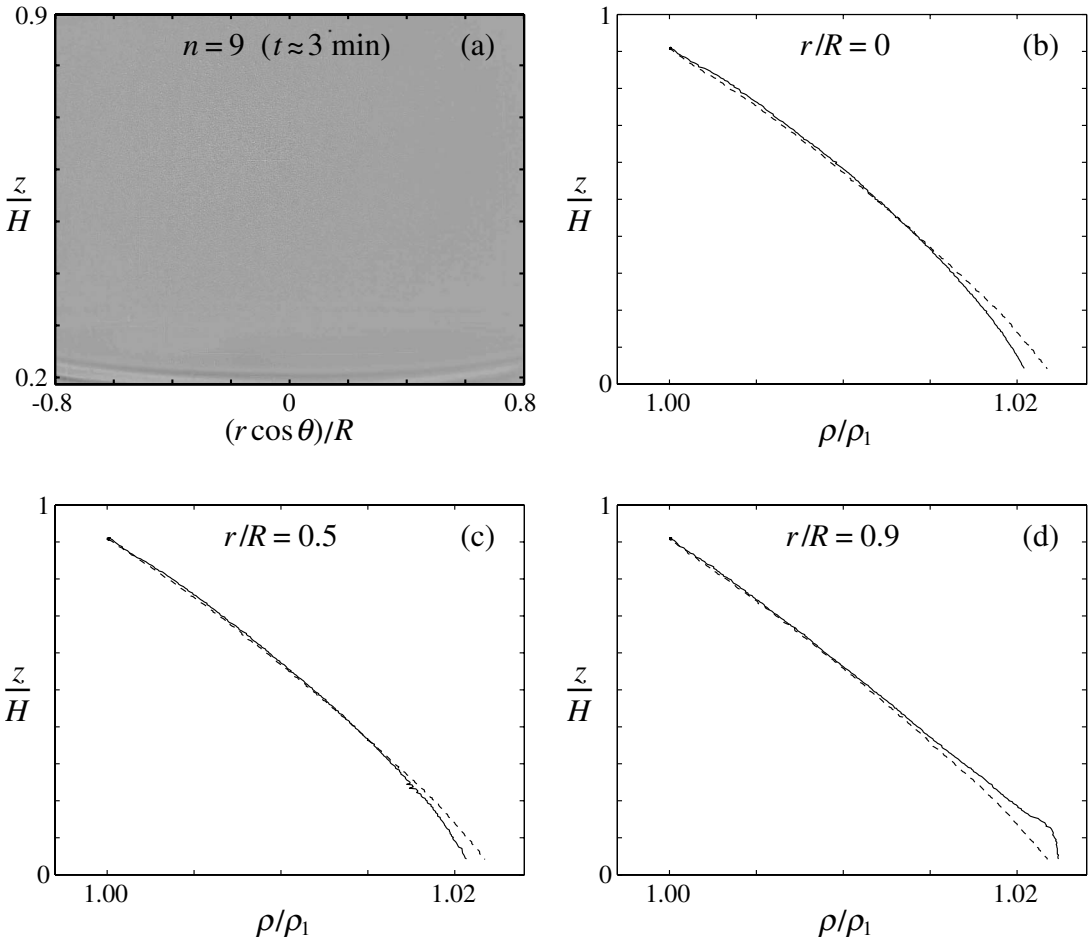

FIG. 3. Measurements obtained from experiment A after $n=(\Omega/2\pi)t=9$ rotation periods. (a) A shadowgraph image obtained during the early stages of the flow development; the homogeneous region shows where the fluid remains unperturbed and (essentially) linearly stratified. [(b)–(d)] A set of measured density profiles obtained at this time, where ρ_1 denotes the value of $\rho_s(r,z)$ at $z=0.9H$; corresponding radial locations $(r/R=0,0.5,0.9)$ are indicated. The initial density profile for the solid rotation state $(t<0)$ is shown by the broken lines.

observed to form only in regions of the interior flow which eventually satisfy this condition, following the initial period of (notably) unsteady flow as the fluid interior adjusts to the onset of disk rotation. Moreover, the staircase density microstructure was observed to form only at times *after* the local flow had reached this balanced state. This is demonstrated by Fig. 7 which shows, for the four experiments listed in Table I, the times at which the flow is (or is not) in balance; here, Eq. (2), in slightly rearranged form, is represented by the horizontal broken line. In all cases, the data shown are taken from the interior point $r/D=0.5$, $z/H=0.52$. Recall the microstructure was observed to form in experiments A and B (represented by $\times$ and +), in which Ro is small, but not in experiments C and D (represented by ● and ○) where $Ro\geq 1$. Consider first experiments A and B. The data for these two experiments $(\times,+)$ show that the flow (at this point) reaches the balanced state after $n\approx 150$ disk rotations. Note, however, in both experiments the density step structures do not become fully formed at this point until much later, i.e., for experiment A after $n\approx 720$ (as shown in Fig. 5). Conversely, the data for experiments C and D (● and ○) show clearly that at no time is either flow in balance at $r/D=0.5$, $z/H=0.52$. Experiment C simply corresponds to the case of weak background rotation (with $Ro=1.0$ and $\Omega\approx 0.1$ rad/s), in which the Coriolis effects are not dominant. Experiment D, in addition, corresponds to the case of relatively strong forcing of the flow by the disk motion (with $Ro=1.9$ and $\Omega_d\approx 1$ rad/s), in which case previous studies[10] have shown (using a setup similar to the one described here) that the induced flow is three-dimensional, exhibiting significant secondary azimuthal wavelike modes.

The density perturbations first develop in the lower region of II (above the interface BB'); Fig. 8 shows a sequence of shadowgraph images, taken at various times throughout experiment A. Initially, two (or three) step structures appear in the form of axisymmetric curved horizontal sheets. As time progresses and the fluid is gradually spun-up, more of the interior region II is destabilized resulting in additional step structures forming further above the interface BB'. Once fully formed, the steplike perturbations have a remarkably regular wavelength and remain robust until they are either entrained through the slowly advancing interface BB', or the table or disk rotation is terminated, and the fluid is spun down. Notably, the step structures do not appear to be unduly affected by the vertical motion of the traversing conductivity probes.

It should be noted that the shadowgraph images can be somewhat misleading, due to the depth-integrated view

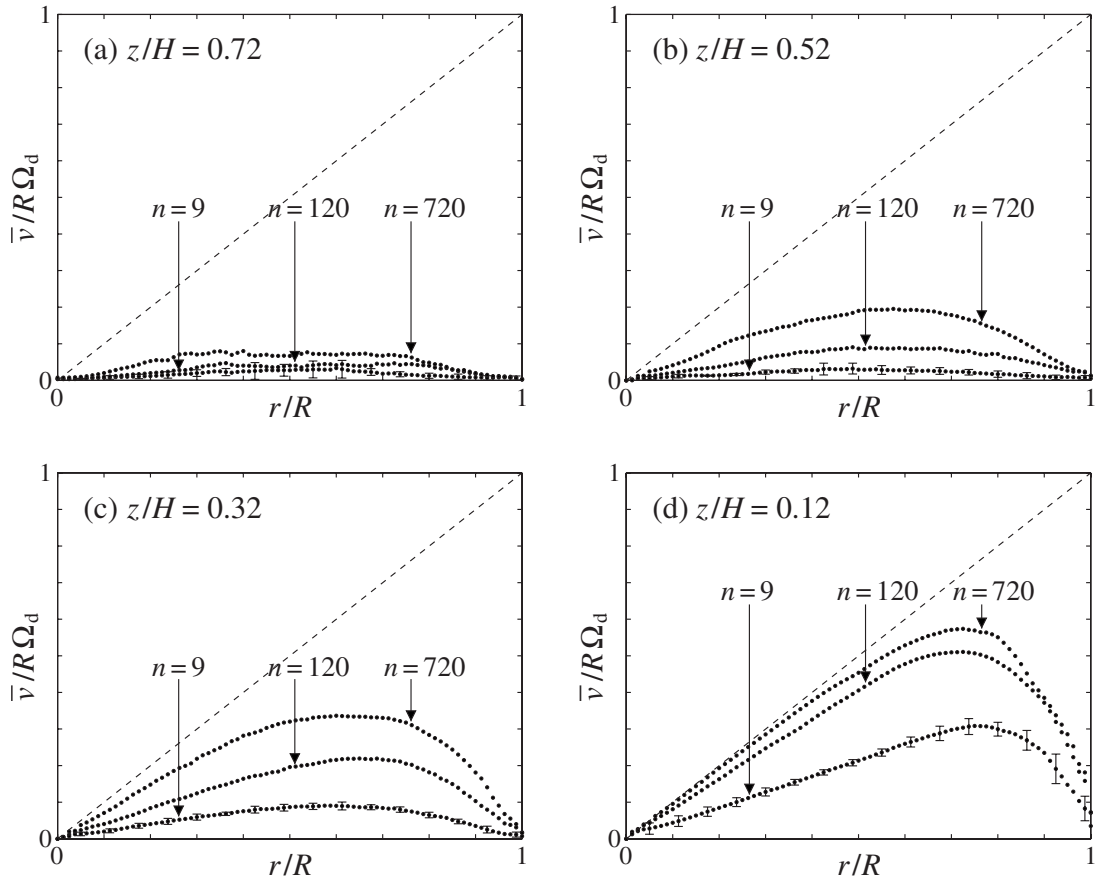

FIG. 4. Experiment A: Measurements of zonal velocity field $\bar{v}(r,z,t)$ at heights $z/H=0.12,0.32,0.52,0.72$; three sets of measurements are included in each plot, obtained after $n=(\Omega/2\pi)t=9$, 120, and 720 rotation periods, as indicated. Error bars are provided in the $n=9$ measurements (every fifth data point) to indicate the typical variation. A similar degree of variation was observed in each of the data. The broken line shows the corresponding disk speed ($r\Omega_d$) at each radial position, and therefore represents the limiting spun-up state.

through the side of the tank. That is, in Figs. 5(a) and 8, the microstructure appears to take the form of axisymmetric, saucer-shaped sheets, extending horizontally across the cylinder. This is not the case. The density measurements show that around the stagnant central axis ($r=0$) the background density field remains unperturbed and essentially linear, as shown by Fig. 5(b). Here, the necessary conditions for the onset of instability are not satisfied in this stagnant region. (This ring-shaped structure of the sheets was also identified by Calman.[14]) However, Fig. 5(b) does show the presence of a weak and smeared density step structure in the interior region II, at $r=0$. These structures were observed in the axial density profiles only during the later stages of the experiment (in this case, $n=720$, i.e., after 4 hours), and several hours after the step structures have formed in the midradius profiles. This manifestation of the density microstructure at $r=0$ is likely to be due to (neglected) nonlinear effects.

Before turning to the stability question, we need to address what is an interesting consequence of the data shown in Fig. 7. Linear spin-up theory (see Refs. 2, 5, and 6, for example) indicates that in the early stages of spin-up, the Ekman flux is $\mathcal{O}(E^{1/2})$ and the meridional velocity components in the fluid interior are also $\mathcal{O}(E^{1/2})$ as a result. That being the case, the terms in the azimuthal vorticity equation not shown in Eq. (2) are very small. Thus, it seems surprising that the data for experiments A and B in Fig. 7 show a large deviation from the balanced state given by Eq. (2) during the initial stages (between $n=0$ and 150 rotation periods) of the flow development. The authors are grateful to an anonymous referee for making this observation. We consider that the reasons for this anomaly go to the inherent nonlinearity of the experiments reported here, for which $Ro=\mathcal{O}(1)$. There is no existing theory for this nonlinear regime, so the orderings are unclear. There are two difficulties. First, the Ekman layer itself is nonlinear, which means that there is no local Ekman suction law analogous to the familiar linear one.[24] The nonlocal character is critical, since now the layer develops from center to rim, with the entire structure nonlinearly coupled to the flow above it. Second, there is the question of the corner eruption of Ekman fluid, a prominent and crucial feature of linear spin-up, first noted by Walin.[5] There is no reason to expect that such an eruption in the nonlinear regime resembles closely that in the linear flow—there will be strong coupling of the corner eruption with the rest of the boundary layer, likely leading to unpredictable *a priori* orderings of the interior flow. (For an example of how complex that coupling can be, the reader is referred to Belcher *et al.*[25] and related papers.) In summary, the clear ordering arguments in linear spin-up depend crucially on the local Ekman suction law; in the absence of such simplified dynamics, the orderings of the interior flow cannot be accomplished with any confidence. In fact, the data of Fig. 7 suggest precisely that there are interior

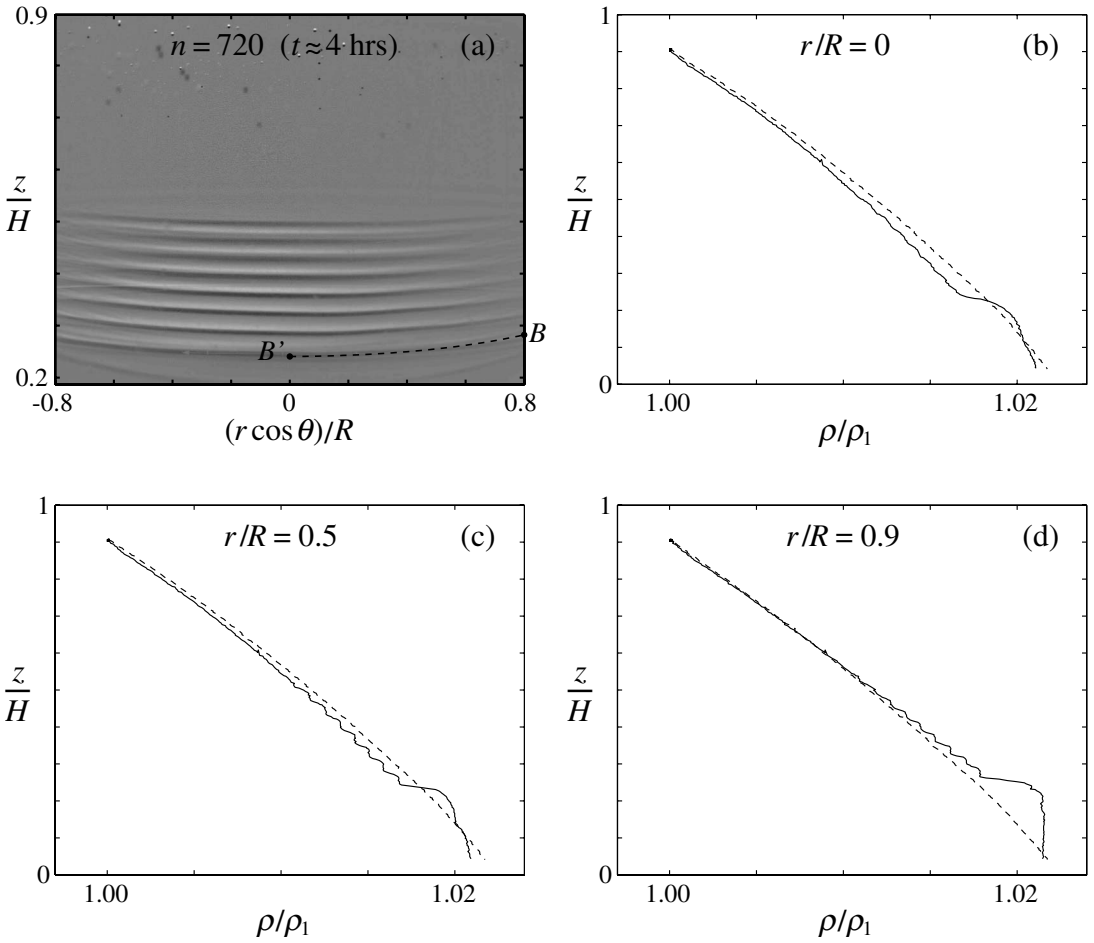

FIG. 5. Experiment A, as in Fig. 3, except that $n=(\Omega/2\pi)t=720$. At this time, region I is fully established across the disk surface, with BB' at $z/H\approx 0.25$.

meridional velocities (during the early stages) that are much larger than $\mathcal{O}(E^{1/2})$, although the detailed measurements of the meridional plane velocity fields that are necessary to confirm this behavior were excluded from consideration in our experiments. While further experiments designed to investigate meridional flow fields are of merit in this regard, we emphasize here that the initial stage of the spin-up process has no real relevance to the core stability analysis we present in this paper. For that reason, we focus henceforth on the later stages when the flow is quasisteady and the instability occurs. Before doing so, however, we note for completeness that an increase in effective viscosity of the fluid (because of

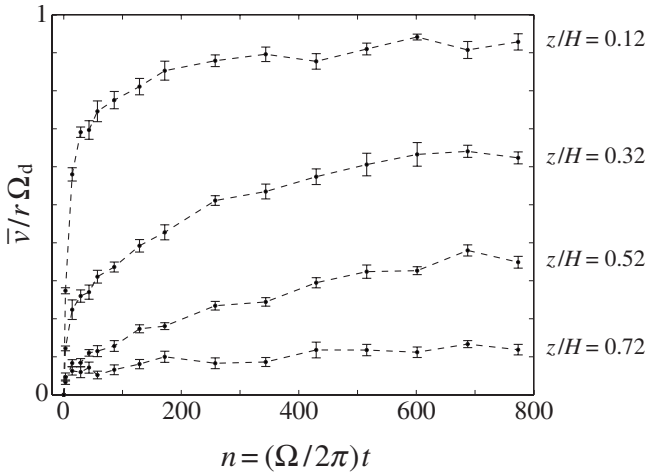

FIG. 6. Experiment A: Plot showing the temporal development of the zonal flow field at $r/R=0.5$. Data are shown for each of the sample heights (as indicated), with the error bars showing the corresponding rms variation.

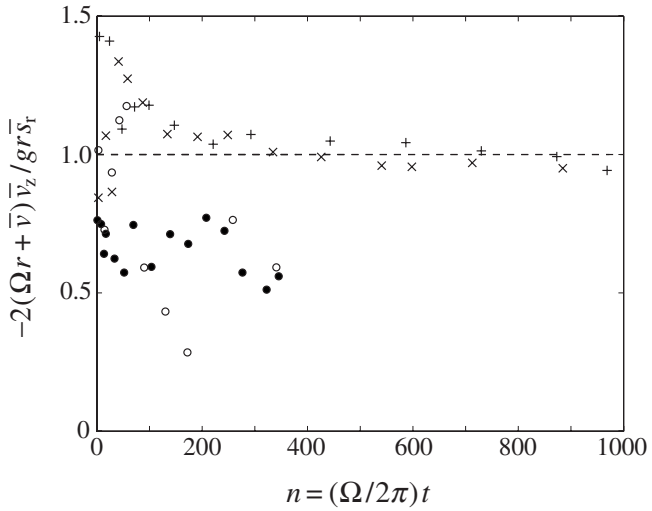

FIG. 7. Plot showing when the four experiments listed in Table I are (or are not) in the balanced state represented by Eq. (2). Note the vertical axis shows the rearranged form $-2(\Omega r+\bar{v})\bar{v}_z/gr\bar{s}_r=1$ of Eq. (2), so that balance is represented by the horizontal broken line. The data shown are from experiments A (×), B (+), C (●), and D (○), all taken from the interior point $r=r_0=0.5R$ and $z=z_0=0.52H$.

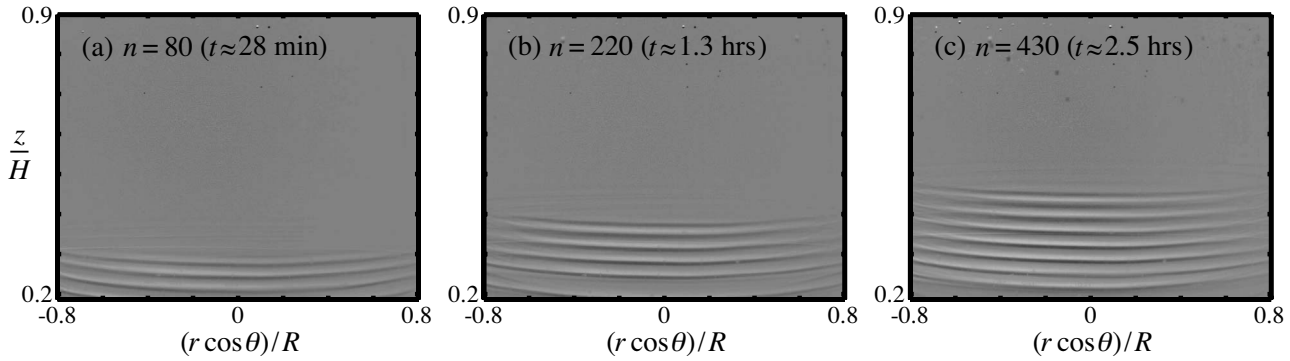

FIG. 8. Experiment A: Sequence of shadowgraph images illustrating the development of the density microstructure in region II.

the presence of tracer particles) has been invoked by the referee as a possible explanation for the imbalance aspect of the initial state behavior outlined above. (Recall that such particles were not present in the experiments used to obtain the density measurements.) However, the viscosity correction in a dilute suspension of small particles is known[26] to be a multiplier of $(1+5\alpha/2)$, where α is the concentration of particles by volume. In our experiments, α is always less than 5×10^{-4}, and so the viscosity correction is clearly negligible for these conditions.

We conclude this discussion by noting that the initial period of rotating-stratified spin-up problems, for $Ro=\mathcal{O}(1)$, is currently not well understood and requires further detailed study.

IV. LARGE-σ CASE

It turns out that one may use asymptotic techniques to considerable advantage to obtain relatively simple results for the most unstable mode. Not only is σ large for the water-salt system, but the numerical values of Θ_1 and Θ_2 are generally large and negative in this series of experiments. Hence, we construct asymptotic solutions for $\sigma\to\infty$, simultaneously with $\Theta_1,\Theta_2\to-\infty$.

If $|\Theta_1|,|\Theta_2|\gg1$, and are both negative (as they are in the experiments), then Eq. (10), written here again for convenience,

$$(\omega+k^2)^2(\omega+k^2/\sigma)+(\mathcal{I}+\mathcal{G})\omega+(\mathcal{I}/\sigma+\mathcal{G})k^2=0, \tag{16}$$

and the fact that $\mathcal{I}$ and $\mathcal{G}$ are both positive for large and negative Θ_1,Θ_2 indicate that there can be no positive real root for ω, since all of the terms are positive. However, we know from McIntyre[3] that the instability that arises at large $\Theta_1\Theta_2$ is monotonic, and it is evident from the experiments that $\Theta_1\Theta_2$ is in fact quite large. The only way that Eq. (16) might exhibit a positive real root is if the multiplier of either the large Θ_1 or Θ_2 terms in $\mathcal{I}$ or $\mathcal{G}$ is small, that is, either $\cos\phi$ or $\sin\phi$ must be small, thereby making either $\mathcal{I}$ or $\mathcal{G}$ negative. So, ϕ must be near 0 or $\pi/2$. It turns out that the latter case is the one that leads to instability.

A. Stability for $\phi=\mathcal{O}(1)$

If $\Theta_1,\Theta_2\to-\infty$, $\sigma\to\infty$, then Eq. (16) becomes, to leading order,

$$(\omega+k^2)^2\omega-(\Theta_1\sin^2\phi+\Theta_2\cos^2\phi)\omega-\Theta_2k^2\cos^2\phi=0, \tag{17}$$

so long as ϕ is such that neither the sine or cosine is small. We have dropped for the moment the $1/\sigma$ terms, since they contribute higher-order corrections to what follows. Then, using the largeness of the three parameters, and assuming that $\omega=\mathcal{O}(1)$, we get to leading order the stable root

$$\omega\sim-\left(\frac{\Theta_2\cos^2\phi}{\Theta_1\sin^2\phi+\Theta_2\cos^2\phi}\right)k^2+\mathcal{O}\left(\frac{1}{\Theta_1},\frac{1}{\Theta_2},\frac{1}{\sigma}\right). \tag{18}$$

Certainly, an asymptotic solution for ω depends on the relative orderings of the three large parameters in this problem, Θ_1, Θ_2, and σ. Nonetheless, a more formal approach than what is presented here shows that, in order to obtain Eq. (18) from Eq. (17), we need require only that $\Theta_1=\mathcal{O}(\Theta_2)$ and $1/\sigma=o(1)$.

The other two roots correspond to large values of ω, and scaling ω with $\sqrt{-\Theta_1}$, construction of a two-term series gives the damped, oscillatory modes

$$\omega\sim\pm i\sqrt{-\Theta_1}\left(\sin^2\phi+\frac{\Theta_2}{\Theta_1}\cos^2\phi\right)^{1/2}-\frac{k^2}{2}\left(\frac{2\Theta_1\sin^2\phi+\Theta_2\cos^2\phi}{\Theta_1\sin^2\phi+\Theta_2\cos^2\phi}\right), \tag{19}$$

for $\Theta_1,\Theta_2\to-\infty$. Once again, since $\sigma\gg1$, the corrections to this expression are higher order.

So, even though the three roots are of differing scales at large $(-\Theta_1)$, none of them leads to an instability of this flow. We now turn to an analysis of the solutions for ω when ϕ is near $\pi/2$.

B. Instability for $\phi \sim \pi/2$

To examine this case, we write

$$\phi = \frac{\pi}{2} + \tilde{\phi}, \quad |\tilde{\phi}| \ll 1,$$

so the parameters that occur in the Eq. (16) take the approximate form

$$\mathcal{I} \sim -\tilde{\phi} - \Theta_1, \quad \mathcal{G} \sim -\tilde{\phi} - \Theta_2 \tilde{\phi}^2, \tag{20}$$

taking $\tilde{\phi}$ to be small and Θ_1 and Θ_2 large and negative. Substituting into Eq. (16) then gives the approximate polynomial in this regime,

$$(\omega + k^2)^2(\omega + k^2/\sigma) - (2\tilde{\phi} + \Theta_1 + \Theta_2\tilde{\phi}^2)\omega - [\tilde{\phi} + \Theta_2\tilde{\phi}^2 + (\tilde{\phi} + \Theta_1)/\sigma]k^2 = 0. \tag{21}$$

Retaining only the dominant terms in the asymptotic limits described above, and for $k = \mathcal{O}(1)$, this equation becomes

$$(\omega + k^2)^2\omega - \Theta_1\omega - (\tilde{\phi} + \Theta_2\tilde{\phi}^2 + \Theta_1/\sigma)k^2 = 0. \tag{22}$$

Then, so long as ω is not large, we get the approximate solution

$$\omega \sim -\left(\frac{\tilde{\phi} + \Theta_2\tilde{\phi}^2 + \Theta_1/\sigma}{\Theta_1}\right)k^2 + \mathcal{O}\left(\frac{1}{\sigma\Theta_1}\right). \tag{23}$$

[The two oscillatory roots, Eq. (19), do not alter dramatically in this regime from those results given above, since putting $\phi = \pi/2$ in that equation clearly does not invalidate those asymptotics.] Now, clearly for $\tilde{\phi}$ sufficiently large, ω goes like $-k^2$, indicating stability. Since the denominator is always negative, the requirement for instability becomes

$$\tilde{\phi} + \Theta_2\tilde{\phi}^2 + \Theta_1/\sigma > 0. \tag{24}$$

This polynomial is positive provided $\tilde{\phi}$ lies between two roots, that is,

$$\tilde{\phi}_- < \tilde{\phi} < \tilde{\phi}_+,$$

where

$$\tilde{\phi}_\pm = -\frac{1}{2\Theta_2} \pm \sqrt{\frac{1}{4\Theta_2^2} - \frac{\Theta_1}{\sigma\Theta_2}}.$$

This range shrinks to zero when the square root vanishes. Thus, for a finite range of $\tilde{\phi}$ that obeys criterion (24), and hence leads to (monotonic) instability, we require

$$\Theta_1\Theta_2 < \frac{\sigma}{4}, \quad k = \mathcal{O}(1). \tag{25}$$

This result agrees with the large-σ limit of McIntyre's result, Eq. (13). Before modifying this result for large k, we note that $\tilde{\phi}$ in the critical range of Eq. (25) is of order $1/\Theta_2$, and is therefore small as initially assumed. Again, formal asymptotics show that result (23) is asymptotically valid for $|\Theta_1| \to \infty$ provided that $\Theta_2 = \mathcal{O}(\Theta_1)$, but also now that $\sigma = \mathcal{O}(\Theta_1\Theta_2)$, which is consistent with our experiments.

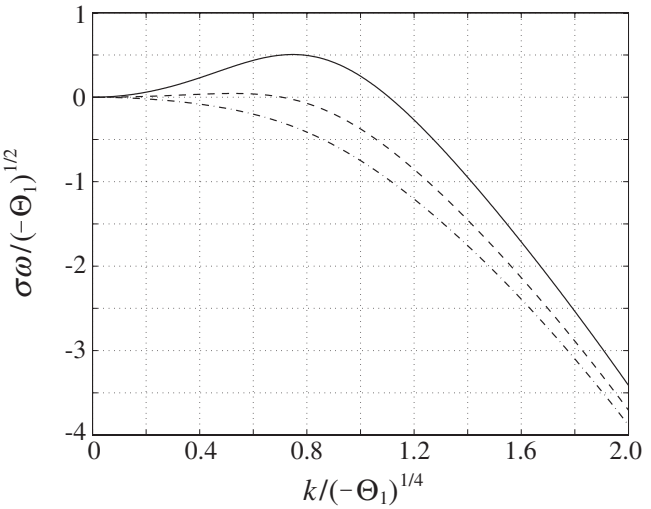

FIG. 9. ω vs k for three values of $\Theta_1\Theta_2/\sigma$ and with $\Psi = -1/2$. The cases shown are: $\Theta_1\Theta_2/\sigma = 0.1$ (solid line), $\Theta_1\Theta_2/\sigma = 0.2$ (dashed line), and $\Theta_1\Theta_2/\sigma = 0.5$ (dotted-dashed line). Recall from Eq. (25) that monotonic instability occurs when $\Theta_1\Theta_2/\sigma < 0.25$.

C. The instability at large k for $\phi \sim \pi/2$

We have found an instability that occurs near $\phi = \pi/2$ whose growth rate is proportional to the square of the wave number, and so grows to larger values as k increases. On the other hand, it is immediately obvious for k sufficiently large that all solutions to Eq. (16) are stable, that is, $\Re\{\omega\} < 0$. Therefore, at some intermediate value of k which evidently must be large, ω passes through zero. We seek in this section to examine the instability in that range of k. We note from Eq. (23) that ω scales with k^2/σ, but from Eq. (21), on the other hand, since ω is smaller than k^2, we obtain a scaling $\omega \sim k^6/(\Theta_1\sigma)$. Balancing these gives $k \sim (-\Theta_1)^{1/4}$ if we take $\sigma = \mathcal{O}(\Theta_1\Theta_2)$ as above. Then, ω is of order $(-\Theta_1)^{-3/2}$. Hence, we now write

$$k = (-\Theta_1)^{1/4}\lambda, \quad \omega = \frac{(-\Theta_1)^{1/2}}{\sigma}\Omega. \tag{26}$$

Substitution into Eq. (21) gives the leading-order result

$$\Omega = -\frac{\lambda^2}{1+\lambda^4}\left[\lambda^4 + \frac{\sigma}{\Theta_1\Theta_2}\left(\Psi + \Psi^2 + \frac{\Theta_1\Theta_2}{\sigma}\right)\right] + \mathcal{O}\left(\frac{1}{\Theta_1}\right), \tag{27}$$

for $\tilde{\phi} = \Psi/\Theta_2$. The instability criterion (25) is recovered if $\lambda^2 \ll 1$.

Since the result (23) is wholly contained in Eq. (27), we can compute ω versus k for a given value of Ψ from Eq. (27). Parametric restrictions here are those of the foregoing $k = \mathcal{O}(1)$ discussion. Typical results are shown in Fig. 9 for both stable and unstable cases. We note that in Eq. (23) the growth rate is order $1/\sigma$, when $k = \mathcal{O}(1)$. However, in this regime, the growth rate is order $(-\Theta_1)^{1/2}/\sigma$, much larger, and so maximum growth rates occur for $k = \mathcal{O}[(-\Theta_1)^{1/4}]$.

Clearly, the maximum growth rate arises when both Ψ and λ derivatives of Ω vanish. That occurs at $\Psi_m=-1/2$ and, after solving a quadratic for λ^4, at

$$\lambda_m^4=\frac{\Phi-3+\sqrt{(1-\Phi)(9-\Phi)}}{2}, \tag{28}$$

where

$$\Phi\equiv\left(1-\frac{\sigma}{4\Theta_1\Theta_2}\right). \tag{29}$$

Substitution into Eq. (27) gives this maximum value of the growth rate as

$$\omega_m\sim\frac{(-\Theta_1)^{1/2}}{\sigma}\left[\frac{3-3\Phi-\sqrt{(1-\Phi)(9-\Phi)}}{\Phi-1+\sqrt{(1-\Phi)(9-\Phi)}}\right]\times\left[\frac{\Phi-3+\sqrt{(1-\Phi)(9-\Phi)}}{2}\right]^{1/2}. \tag{30}$$

The associated wave number is given by

$$k_m\sim\left\{-\frac{\Theta_1}{2}[\Phi-3+\sqrt{(1-\Phi)(9-\Phi)}]\right\}^{1/4}, \tag{31}$$

which is real only for $\Phi<0$, and that occurs if Eq. (25) is satisfied.

To summarize then, the most unstable mode of form (9) is

$$\exp\left[i(-\Theta_1)^{1/4}\lambda_m\left(y+\frac{x}{2\Theta_2}\right)+\omega_m\tau\right], \tag{32}$$

where this asymptotic result is valid for

$$\Theta_1,\Theta_2\to-\infty \quad \text{and} \quad \sigma=\mathcal{O}(\Theta_1\Theta_2). \tag{33}$$

In dimensional form, the characteristic vertical length scale (L) and time scale (T) for this most unstable mode are given by

$$L=\frac{2\pi}{k_m}\left(\frac{\nu^2}{g\beta\bar{s}_r^0}\right)^{1/4} \quad \text{and} \quad T=\frac{2\pi}{\omega_m}\left(\frac{1}{g\beta\bar{s}_r^0}\right)^{1/2}. \tag{34}$$

D. Comparison with experiment

Theoretical predictions were compared with measurements from the experiment data at $r_0/R=0.5$, $z_0/H=0.52$. At this interior point, the measured density and zonal velocity fields (and associated gradients) were not unduly affected by the advancing frontal region, or by the tank sidewall. Moreover, this point provided a period of at least 1 hour before the flow became unstable, allowing the corresponding onset time for the instability to be determined. This is illustrated by Fig. 10, which shows $\Theta_1\Theta_2$ plotted against n for experiments A and B. Also shown are the conditions for monotonic and oscillatory instability; the latter is obtained directly from Eq. (14), by taking the $\sigma\gg1$ limit. (Note that in all experiments considered here, and as illustrated in Fig. 10, the condition for oscillatory modes was never satisfied.) When Figs. 7 and 10 are compared, we see that it takes around $n=200$ rotation periods for the flow in experiments A and B to reach approximate gradient wind balance (i.e., about 70 and 40 min, respectively).

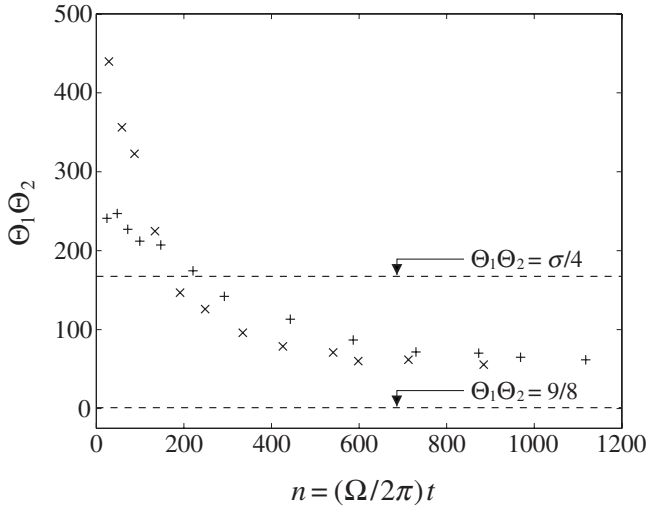

FIG. 10. Plot showing $\Theta_1\Theta_2$ plotted against dimensionless time n for Experiments A (×) and B (+); all data shown are taken from the interior point $r=r_0=0.5R$, $z=z_0=0.52H$. Also shown are the $\sigma\gg1$ conditions for monotonic instability ($\Theta_1\Theta_2<\sigma/4$) and oscillatory instability ($\Theta_1\Theta_2<9/8$).

It is possible to compute $\Theta_1\Theta_2$ from linear, spin-up theory, of the kind reviewed elsewhere,[2] and then compare with the experimentally obtained product shown in Fig. 10. However, there is a serious difficulty with such a comparison: the linear spin-up theory requires $Ro\ll1$, and in the initial stages of the spin-up, due to the corner eruption, $Ro\ll E^{1/2}$, where $E=\nu/\Omega H^2$ is the Ekman number (which is about 5×10^{-5} in our experiments). In fact, here, $Ro\gg E^{1/2}$. Of all the small parameters that are relevant to such an analysis (viz., $Ro, E^{1/2}, \sigma^{-1}$), the Rossby number is by far the largest. After temporal adjustments have occurred, and for the case for which $\sigma Ro\gg1$ (as in these experiments), though the gradient wind balance remains approximately linear, the equations for the zonal velocity component and the density perturbation are inherently nonlinear. Salinity perturbations near the boundary, in a layer of width $E^{1/2}/(\sigma Ro)^{1/3}$, drive similar perturbations in the thicker ($E^{1/2}$) Ekman layer, and that induces a nonzero salinity perturbation in the interior.

We denote by L_{exp} the height (or wavelength) of the fully developed density step structure observed in the experiments, measured directly from the midradii density profiles at the point (r_0,z_0). This step height was compared with the corresponding vertical perturbation length scale L predicted by the theory. The results for experiments A and B are given in Table II. Once fully developed, the height of the density

TABLE II. Predicted and measured values of perturbation length and time scales for experiments A and B.

Experiment label	L (cm)	L_{exp} (cm)	T (hours)	T_{exp} (hours)
A	1.04 ± 0.09	1.10 ± 0.11	4.3 ± 0.7	5.0 ± 0.3
B	0.82 ± 0.04	0.80 ± 0.09	2.4 ± 0.8	3.1 ± 0.3

step was observed to remain essentially constant. Hence, each value of L_{exp} was an average value calculated from the period after the density step had fully formed; typically, this average was taken from between six and eight individual measured values, obtained over a period of between 2 and 3 hours. The corresponding rms values are also shown to indicate the typical variation over this period. Likewise, the values of L shown in Table II are averaged values. Recall that the length scale L is calculated using Eq. (34), and so the background flow conditions $(\Theta_1, \Theta_2, \sigma, \delta_1)$ at (r_0, z_0) must be used. The quasisteady nature of the background flow, clearly illustrated by Figs. 7 and 10, means that the values of L exhibit a degree of slow-time variation. However, in all cases considered here, the calculated values were found to become essentially constant, and always well *before* the time at which the step structure is observed to be fully formed. Hence, the values of L shown in Table II are the average taken from this near-constant period; again, rms values are included to indicate the typical variation observed. Clearly, the correspondence between experiment and theory is very good, especially bearing in mind that the stability analysis is linear and that the height of the density steps observed in the experiments do not represent very small perturbations from the linear initial state. A similar degree of correspondence was found in the other experiments in which the instability was observed to form.

Table II also shows the time scale T calculated, using Eq. (34), for experiments A and B. For the same reasons outlined above, the values of T shown are averages (taken over the same period used to average L). Again, rms values are included to show the typical variability. Of course, the corresponding e-folding time scale could not be measured directly from the experiment data. Hence, the growth time scale for the experiments, henceforth denoted T_{exp}, was defined as the time from when the condition for instability is first satisfied to when the density step structure was first observed to be fully developed. The corresponding values are also shown in Table II; the confidence intervals of 0.3 hours are based on the typical sampling frequency of the density probes during the latter stages of the experiment. Despite the comparatively arbitrary way in which T_{exp} has been defined, the agreement between the time scales is good. Of course, one would expect T_{exp} to be several times larger than the e-folding time T for the most unstable mode.

It is also observed that the values of the product $\Theta_1\Theta_2$ are larger at larger values of z. Hence, in general, the instability is observed to form in the lower portion of the tank. This is indeed what one sees in our experiments, as illustrated by Figs. 5 and 8. Moreover, as one moves upward through the unstable region toward the critical value $\Theta_1\Theta_2 = \sigma/4$ (so that $|\Phi| \to 0$, where recall $\Phi < 0$ in this unstable region), the wavenumber (k_m) and growth rate (ω_m) of the most unstable mode decrease toward zero. According to Eqs. (30) and (31) this decrease goes like

$$k_m \sim \left(\frac{\Theta_1\Phi}{3}\right)^{1/4} \quad \text{and} \quad \omega_m \sim -\left(\frac{2^{3/2}\Phi}{3\sigma}\right)k_m^2, \tag{35}$$

when $|\Phi| \to 0$ (with $\Phi < 0$).

V. SUMMARY AND FINAL REMARKS

Experiments were performed on a linearly salt-stratified water solution ($\sigma \approx 670$) in a cylindrical container that was initially in a state of solid-body rotation. Relative fluid motion was induced by a disk positioned at the container base, and set to rotate independently of the container and cyclonically. The disk rotation results in the formation of two distinct regions of flow (Fig. 2). Initially, a layer of well-mixed fluid is observed to form in the high-shear region immediately above the disk surface, within which the fluid is essentially spun-up [region I, Fig. 2(b)]. In addition, Ekman suction acts to stretch the background vorticity, thereby establishing a zonal shear flow within the interior fluid above [region II, Fig. 2(b)]. Notably, the background stratification remains essentially linear, albeit deformed by the stretching effect; the mixed-layer interface is observed to migrate slowly upward through the fluid interior. Our experiments focused on analyzing the stability of the axisymmetric zonal flow within this interior region.

It was found that only when the local flow conditions were in the (near-steady) balanced state was the interior region destabilized by the viscous overturning mechanism first proposed by McIntyre.[3] This instability is identified through the formation of a steplike density perturbation to the near-linear background density gradient. The step structures are first observed to form in the lower part of region II (above the interface BB'), and take the form of curved nearly horizontal ring-shaped sheets. As time progresses the zonal flow within region II increases so that more of the interior becomes unstable, resulting in additional step structures forming further above the interface BB'. Once fully formed, the step structures appear to have a near-constant wavelength. Moreover, the step structures remain robust until they are entrained through the slowly advancing interface BB' (or until the table rotation is terminated and the fluid spun down).

The instability criterion, derived from conventional normal mode analysis, is shown to be dependent on the dimensionless parameters σ, Θ_1, and Θ_2, the latter depending on the local values of the vertical and radial gradients of the background density and zonal velocity fields. These quantities were measured in each experiment using a combination of zonal-plane PIV and a radial array of traversing conductivity probes. The data obtained confirmed that the instability criterion (viz., $\Theta_1\Theta_2 < \sigma/4$ for $\sigma \gg 1$) does indeed predict when the interior region is unstable (see Fig. 10). The simple linear theory provides criteria for both monotonic and oscillatory instability. However, in our experiments only monotonic modes were observed (as shown in Fig. 10).

By using the fact that $\sigma, \Theta_1\Theta_2 \gg 1$, simple asymptotic expressions for the maximum growth rate and associated wave number were derived from the cubic dispersion relation. The predicted perturbation length scales L were compared with the corresponding wavelength L_{exp} of the step structures measured directly from the midradii density profiles. Over the range of experiment conditions considered here, the agreement was found to be very good, where in all cases $(L_{exp}/L) \approx 1.0$–1.3, where typically, $L_{exp} \approx 1$ cm.

Likewise, the predicted and measured perturbation time scales were compared, where in all cases $(T_{\mathrm{exp}}/T) \approx 1.1-2.1$. Here, T_{exp} was defined as the growth time of the fully developed step structure (typically of the order several hours), which one would expect to be several times larger than the e-folding time for the most unstable mode.

Finally, we have determined, as noted earlier, that the inherent nonlinearity of the base flow in this problem, owing to Rossby numbers that are much larger than any other small parameter in the problem, means that comparisons with linear spin-up theory[2] are meaningless. That difficulty appears in two ways in this paper. First, nonlinearity of the underlying flow makes it impossible, short of full numerical solution, to obtain a sensible long-time limit for $\Theta_1\Theta_2$, for comparison with the asymptote evident in Fig. 10. In Spence *et al.*,[6] good agreement between experiment and theory was found, for example, for v versus t at particular (r,z) locations, but there $Ro/E^{1/2}$ is order one. So, second, similar linear-theory comparisons with the data of Fig. 6 are also meaningless, for precisely the same reasons, and so have not been included here. The point of this paper is, in fact, not comparison of experiment and theory for the spin-up itself, but comparison of stability theory with results of the experiments.

ACKNOWLEDGMENTS

The authors acknowledge the support of the U.K. Engineering and Physical Sciences Research Council (EPSRC) Physics/Engineering Programme through the award of Grant No. GR/R74703101.

[1] E. R. Benton and A. Clark, "Spin-up," Annu. Rev. Fluid Mech. **6**, 257 (1974).
[2] P. W. Duck and M. R. Foster, "Spin-up of homogeneous and stratified fluids," Annu. Rev. Fluid Mech. **33**, 231 (2001).
[3] M. E. McIntyre, "Diffusive destabilization of the baroclinic circular vortex," Geophys. Fluid Dyn. **1**, 19 (1970).
[4] M. E. McIntyre, "Role of diffusive overturning in nonlinear axisymmetric convection in a differentially heated rotated annulus," Geophys. Fluid Dyn. **1**, 59 (1970).
[5] G. Walin, "Some aspects of time-dependent motion of a stratified rotating fluid," J. Fluid Mech. **36**, 289 (1969).
[6] G. S. Spence, M. R. Foster, and P. A. Davies, "The transient response of a contained rotating stratified fluid to impulsively started surface forcing," J. Fluid Mech. **243**, 33 (1992).
[7] J. Pedlosky, "An overlooked aspect of the wind-driven ocean circulation," J. Fluid Mech. **32**, 809 (1968).
[8] P. F. Linden and G. J. F. van Heijst, "Two-layer spin-up and frontogenesis," J. Fluid Mech. **143**, 69 (1984).
[9] J.-B. Flór, M. Ungarish, and J. W. M. Bush, "Spin-up from rest in a stratified fluid: Boundary flows," J. Fluid Mech. **472**, 51 (2002).
[10] R. J. Munro and P. A. Davies, "The flow generated in a continuously stratified rotating fluid by the differential rotation of a plane horizontal disc," Fluid Dyn. Res. **38**, 522 (2006).
[11] F. Y. Moulin and J.-B. Flór, "On the spin-up by a rotating disk in a rotating stratified fluid," J. Fluid Mech. **516**, 155 (2004).
[12] R. C. Kloosterziel, "Surface forced internal waves and vortices in uniformly stratified and rotating fluids," J. Fluid Mech. **421**, 39 (2000).
[13] D. J. Baker, "Density gradients in a rotating stratified fluid: Experimental evidence for a new instability," Science **172**, 1029 (1971).
[14] J. Calman, "Experiments on high Richardson number instability of a rotating stratified shear flow," Dyn. Atmos. Oceans **1**, 277 (1977).
[15] K. Hedstrom and L. Armi, "An experimental study of homogeneous lenses in a stratified rotating flow," J. Fluid Mech. **191**, 535 (1988).
[16] J. M. H. Fortuin, "Theory and application of two supplementary methods of constructing density gradient columns," J. Polym. Sci., Polym. Phys. Ed. **44**, 505 (1960).
[17] C. Oster, "Density gradients," Sci. Am. **213**, 70 (1965).
[18] M. J. Head, "The use of miniature four-electrode conductivity probes for high resolution measurement of turbulent density or temperature variations in salt-stratified water flows," Ph.D. dissertation, University of California, San Diego, 1983.
[19] As of May 2010, available at Dalziel Research Partners, 142 Cottenham Road, Histon, Cambridge CB24 9ET, United Kingdom.
[20] P. A. Davies, "Aspects of flow visualisation and density field monitoring of stratified flows," Opt. Lasers Eng. **16**, 311 (1992).
[21] V. Barcilon and J. Pedlosky, "On the steady motions produced by a stable stratification in a rapidly rotating fluid," J. Fluid Mech. **29**, 673 (1967).
[22] H. P. Greenspan, *The Theory of Rotating Fluids* (Cambridge University Press, Brookline, 1968).
[23] V. W. Ekman, "On the influence of the Earth's rotation on ocean-currents," Ark. Mat., Astron. Fys. **2**, 1 (1905).
[24] D. A. Bennetts and L. M. Hocking, "On nonlinear Ekman and Stewartson layers in a rotating fluid," Proc. R. Soc. London, Ser. A **333**, 469 (1973).
[25] R. J. Belcher, O. R. Burggraf, and K. Stewartson, "On generalized-vortex boundary layers," J. Fluid Mech. **52**, 753 (1972).
[26] G. K. Batchelor, *An Introduction to Fluid Mechanics* (Cambridge University Press, Cambridge, 1967).